Lift and Drag Behavior of Unconstrained Bluff Bodies

Scott M. Murman

Scott.M.Murman@nasa.gov

NASA Ames Research Center, Moffett Field, CA, USA

Abstract

A method for predicting the drag of unconstrained bluff bodies from subsonic through supersonic flight conditions using analytic expressions is presented. The method is motivated by the need to rapidly analyze the trajectories of potential debris sources for the Space Shuttle Launch Vehicle. Comparisons are presented against both fully-coupled inviscid 6-DOF simulation results, and validated drag predictions for the drag experienced by insulating foam shed from the shuttle external tank.

1 Introduction

This paper is chiefly concerned with predicting the lift and drag characteristics of unconstrained bodies traveling at speeds up to Mach 10 within the Earth's atmosphere. The motivation for this work is the rapid assessment of potential debris sources (insulating foam, ice, ...) for the Space Shuttle Launch Vehicle (SSLV), however the analysis is general and can be applied to a variety of problems. Figure 1 presents a gallery of shapes analyzed during the space shuttle Return-to-Flight (RTF) initiative. Unlike vehicles designed for controlled flight, these general shapes cannot maintain an aerodynamically efficient (trim) orientation, i.e. they are not stable in a low-drag/high-lift orientation.* Further, in supersonic flow a general body will often have a static stability point in a bluff-body orientation. Hence, the aerodynamic analysis for general unconstrained shapes reduces to analyzing the behavior of bluff bodies.

2 Drag

The first aerodynamic parameter required to characterize the behavior of debris shapes is the drag coefficient. This is used with a ballistic code to estimate the position and

*Some shapes, such as spheres or cubes, may be stable in their lowest drag orientation, however they will not generate appreciable lift.

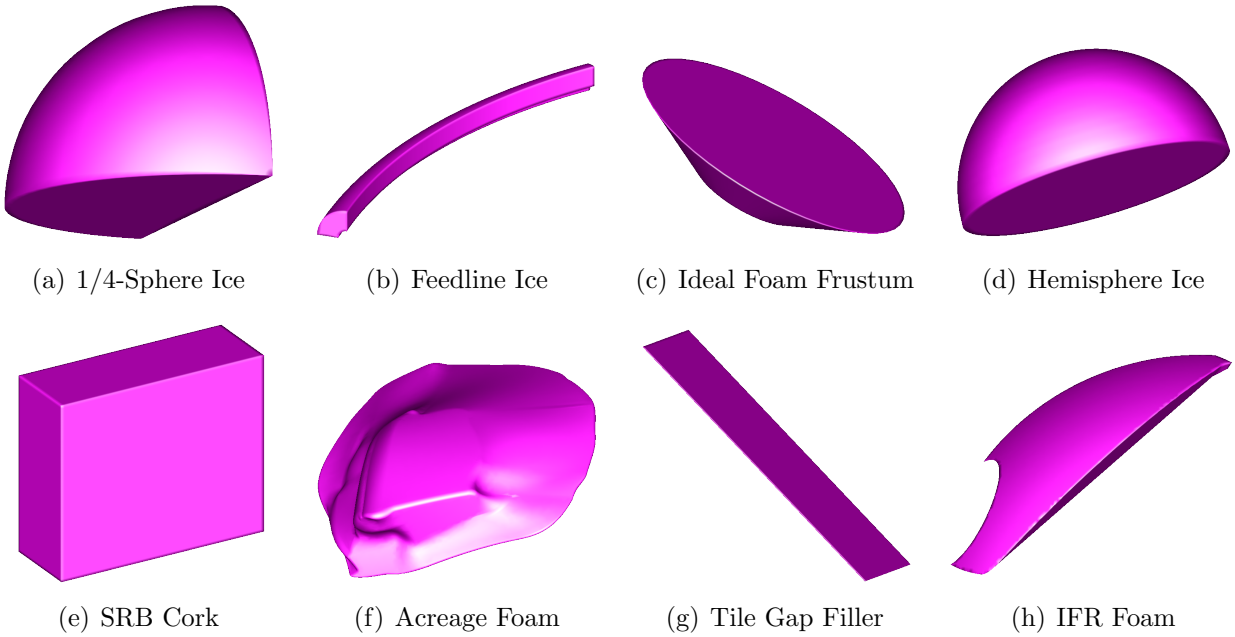

(a) 1/4-Sphere Ice (b) Feedline Ice (c) Ideal Foam Frustum (d) Hemisphere Ice

(e) SRB Cork (f) Acreage Foam (g) Tile Gap Filler (h) IFR Foam

Figure 1: Gallery of debris shapes analyzed during NASA's Return-to-Flight initiative.

velocity along a direction of travel. Excursions from this direction are determined by the aerodynamic lift, and are considered in the next section. Figures 2 and 3 present computed streamlines around a bluff body (parallelepiped) for two body aspect ratios, in subsonic and supersonic flow respectively. As the aspect ratio of the body increases, the region around the body governed by one-dimensional flow also increases, to the point where a one-dimensional analysis can provide an accurate estimate of the pressure on the majority of the area for the windward and leeward faces. Since we are only interested in analyzing bluff bodies, which by definition have the largest body dimension perpendicular to the flow direction, the contribution of skin friction to drag is negligible. Similarly, the Reynolds number at 200,000 ft. of altitude during ascent of the SSLV is still $\mathcal{O}(10^2)$ for a body of dimension 1 inch, and hence low Reynolds number effects can be neglected. The approach here is thus not to directly predict the drag for any body shape, but rather predict how the drag differs from the asymptotic behavior for a 3-D bluff body of infinite aspect ratio.

2.1 Subsonic

In a compressible, subsonic flow (here defined as $0.1 \leq M_\infty \leq 0.8$) the pressure on the windward wall (p_w) can be estimated using the 1-D isentropic flow relationship for stagnation pressure (cf. [2])

$$\frac{p_w}{p_\infty} = \left(1 + \frac{\gamma - 1}{2} M_\infty^2\right)^{\frac{\gamma}{\gamma - 1}} \tag{1}$$

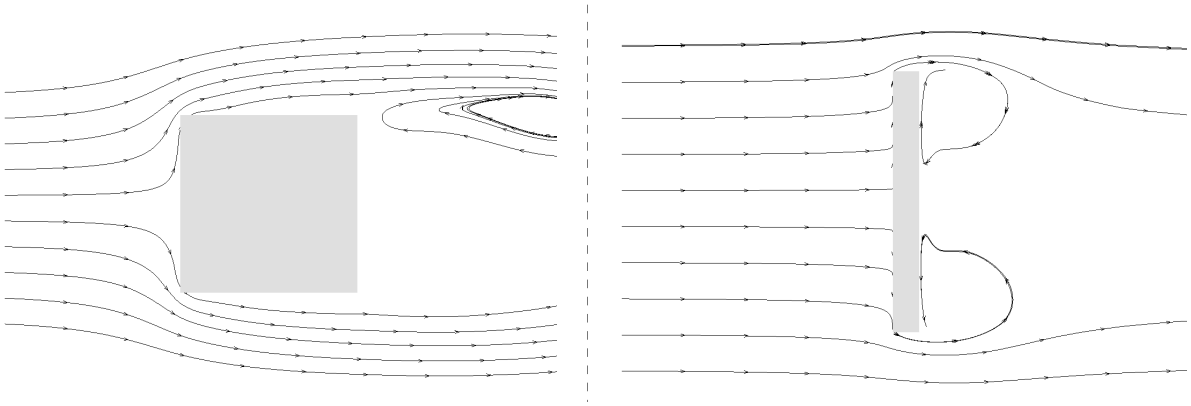

(a) Aspect ratio = 1 (b) Aspect ratio = 10

Figure 2: Effect of aspect ratio on the subsonic flow around a bluff body.

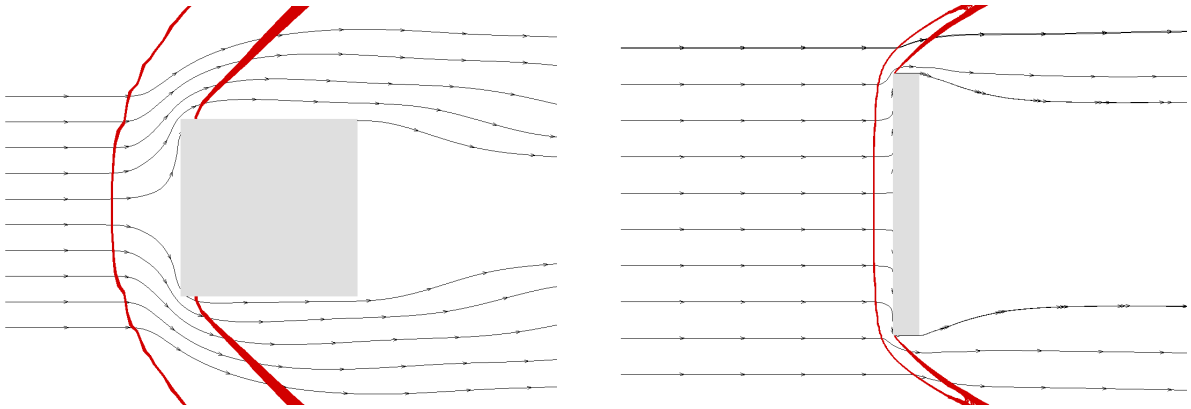

(a) Aspect ratio = 1 (b) Aspect ratio = 10

Figure 3: Effect of aspect ratio on the supersonic flow around a bluff body.

The pressure on the leeward wall face is approximated as

$$\frac{p_b}{p_\infty} = 1.0 \tag{2}$$

While these provide reasonable estimates over a large portion of the surface area, a correction term to account for 3-D effects can improve the integrated drag prediction. This correction is assumed proportional to the square of the Mach number to leading order, so that $\frac{p_c}{p_\infty} \sim M_\infty^2$. Comparison against inviscid computed results provides the coefficient for this scaling

$$\frac{p_c}{p_\infty} = \frac{\gamma}{5} M_\infty^2 \tag{3}$$

Combining the above wall pressures and correction, along with the dynamic pressure ($\frac{1}{2}\gamma p_\infty M_\infty^2$) provides the following estimate for the drag coefficient of a bluff body with high

aspect ratio in the subsonic regime

$$C_D = \frac{\left[\left(1 + \frac{\gamma-1}{2}M_\infty^2\right)^{\frac{\gamma}{\gamma-1}} - \left(1.0 - \frac{\gamma}{5}M_\infty^2\right)\right] A}{\frac{1}{2}\gamma M_\infty^2 S} \tag{4}$$

where A is the frontal area of the body, and S is a suitable reference area.

2.2 Supersonic

The drag in the supersonic regime, here defined as $2 \leq M_\infty \leq 10$, can be predicted in a similar manner as the subsonic regime. A bow shock forms ahead of the bluff body, which approaches a normal shock as the aspect ratio increases (cf. Fig. 3). The pressure and Mach number behind the shock can thus be predicted from the shock jump relations

$$\frac{p_s}{p_\infty} = 1 + \frac{2\gamma}{\gamma+1}\left(M_\infty^2 - 1\right) \tag{5}$$

$$M_s^2 = \frac{(\gamma-1)M_\infty^2 + 2}{2\gamma M_\infty^2 - (\gamma-1)} \tag{6}$$

Behind the shock there is an isentropic compression governed by Eqn. 1. The wall pressure is thus predicted by

$$\frac{p_w}{p_\infty} = \left[1 + \frac{2\gamma}{\gamma+1}\left(M_\infty^2 - 1\right)\right]\left[1 + \frac{\gamma-1}{2}\frac{(\gamma-1)M_\infty^2 + 2}{2\gamma M_\infty^2 - (\gamma-1)}\right]^{\frac{\gamma}{\gamma-1}} \tag{7}$$

The back pressure behind the body is approximated as approaching vacuum, i.e. $p_b = 0$. As with the subsonic regime, a 3-D correction term proportional to the square the Mach number is determined from comparison against computed inviscid results. This correction term is

$$\frac{p_c}{p_\infty} = -\frac{\gamma}{10}M_\infty^2 \tag{8}$$

The drag coefficient thus becomes

$$C_D = \frac{\left\{\left[1 + \frac{2\gamma}{\gamma+1}\left(M_\infty^2 - 1\right)\right]\left[1 + \frac{\gamma-1}{2}\frac{(\gamma-1)M_\infty^2+2}{2\gamma M_\infty^2-(\gamma-1)}\right]^{\frac{\gamma}{\gamma-1}} - \frac{\gamma}{10}M_\infty^2\right\} A}{\frac{1}{2}\gamma M_\infty^2 S} \tag{9}$$

2.3 Transonic

In the transonic regime ($1.0 \leq M_\infty \leq 1.2$) the windward wall pressure can again be predicted with the isentropic stagnation pressure, Eqn. 1. The leeward wall pressure is

approximated with a constant value, $\frac{p_b}{p_\infty} = \frac{1}{4}$. The quadratic correction term is $\frac{p_c}{p_\infty} = -\frac{\gamma}{10}M_\infty^2$. The drag coefficient becomes

$$C_D = \frac{\left[\left(1+\frac{\gamma-1}{2}M_\infty^2\right)^{\frac{\gamma}{\gamma-1}} - \left(\frac{1}{4}+\frac{\gamma}{10}M_\infty^2\right)\right]A}{\frac{1}{2}\gamma M_\infty^2 S} \tag{10}$$

The drag coefficient variation is assumed linear in the model gaps around the transonic region.

The drag coefficient predictions outlined above are compared to inviscid computations for 3-D parallelepiped shapes of increasing aspect ratio and unit depth in Fig. 4, using $S = A$. As the aspect ratio increases, the computed drag coefficient is in good agreement with the model. For unconstrained trajectories, the uncertainty in the dynamic behavior (e.g. oscillating vs. tumbling) swamps the uncertainty in aspect ratio in Fig. 4, hence the effect of aspect ratio is subsumed into the dynamic analysis to follow. For completeness, the following corrections are effective for static configurations when the frontal area can be accurately determined. In the subsonic region, the correction term can be altered as

$$\frac{p_c}{p_\infty} = \frac{\gamma}{25}M_\infty^2\left(5 - \frac{4}{\sqrt{AR}}\right) \tag{11}$$

The correction term in the supersonic region becomes

$$\frac{p_c}{p_\infty} = -\frac{\gamma}{10}M_\infty^2\left(1 + \frac{1}{AR}\right) \tag{12}$$

The transonic region is left for future work.

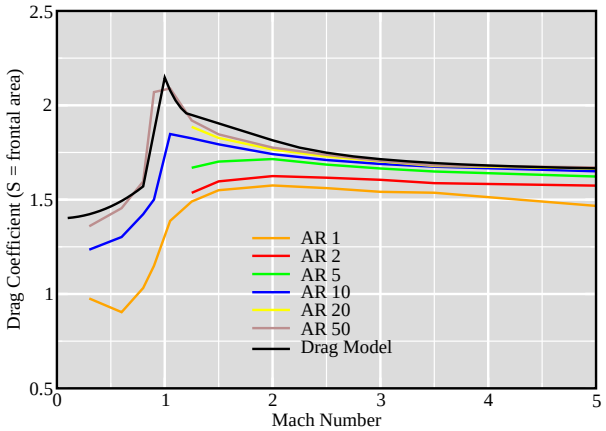

Figure 4: Drag model for flow around a high aspect ratio bluff body.

2.4 Dynamic Behavior

The dynamic behavior of an unconstrained bluff body is a complex unsteady phenomena. Roughly, we can break the behavior into two modes: a tumbling motion, and an unsteady oscillation about a stability point (cf. [1]). The type of motion is difficult to predict in general, depending upon the body shape and orientation, the initial angular rate, the ratio of material to air density, etc. The details of the dynamic drag variation for a single trajectory is similarly complex, and characterized by large changes in magnitude as the body orientation changes. The approach here follows [1]; first develop upper and lower bounds on the drag variation, then focus on nominal or stochastic models.

The dynamic modeling determines an appropriate "effective" aerodynamic frontal area, A, to use in the drag models (Eqns. 4, 9, and 10). This effective area is essentially a static projection of the rotating total area onto the direction of the velocity vector, i.e. dynamic effects such as hysteresis are ignored. In Fig. 4 the effective frontal area is also specified as the reference area in the drag coefficient. While this is ideal, it is difficult to achieve in practice for general shapes, which may have multiple stability points or preferred axes of rotation. A practical alternative is to consider the reference area S as the total wetted area of the body, and then seek an effective bounding area ratio $\frac{A}{S}$.

Figure 5a presents the exposed frontal area variation for a bluff body rotating about a fixed axis at a constant rotation rate ω. Rotation at a constant rate is considered a limiting behavior. The frontal area varies sinusoidally at a frequency of 2ω between the maximum and minimum areas. This ideal is a reasonable representation of the behavior of general rotating bodies. The exposed frontal area for a similar bluff body oscillating with angular rate ω about a stability point is presented in Fig. 5b. The amplitude of the oscillation is represented by the area A_o. As with constant rotation, the frontal area varies sinusoidally between a maximum and minimum with frequency 2ω. As a practical limit, the minimum drag orientation for an oscillating body is the minimum frontal area ("edge-on") configuration. Hence, when considering the extreme behavior, tumbling and oscillation are characterized similarly. If we define the effective aerodynamic area as the average area over a cycle of motion then the largest possible effective area is the maximum area (statically-stable orientation), and the minimum is one half the sum of the maximum and minimum areas. If we consider the limit where the minimum edge-on area approaches zero then we see that the bounding effective areas simplify to the maximum frontal area, and one half the maximum frontal area.

As with the drag model development, parallelepiped shapes are used to simplify the analysis of the effective area ratio. Based on the bounding analysis above, we only need to estimate the ratio of the maximum possible frontal area to the total area. For a parallelepiped, the total area is given by

$$S = 2ARh^2 + 2ARht + 2ht \tag{13}$$

where h is the height of the piece perpendicular to the velocity vector, and t is the dimension in the wind direction. By our definition of a bluff-body flow configuration, $t \leq h$, hence we

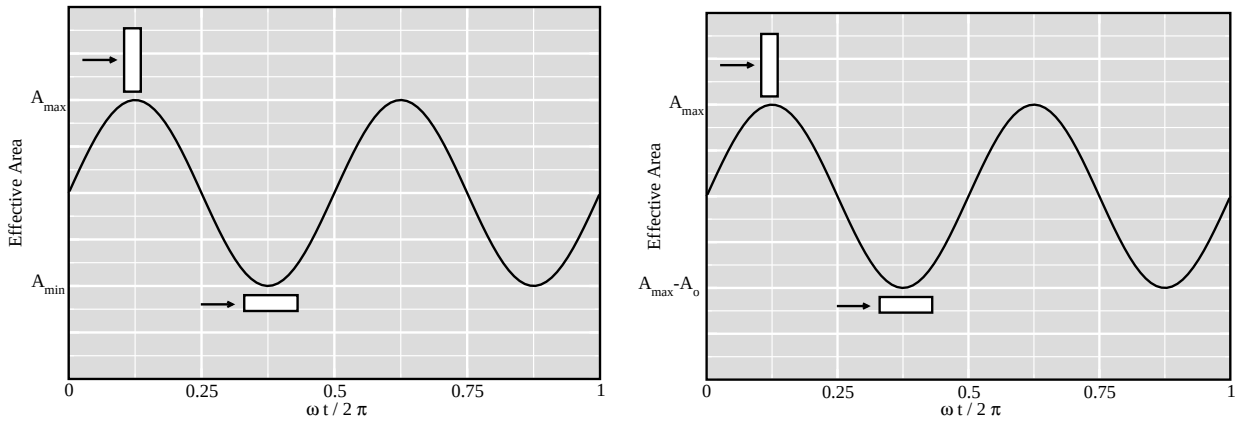

(a) Rotating (b) Oscillating

Figure 5: Idealized sinusoidal variation of frontal area for dynamic trajectories.

have two limiting configurations: $t \ll h$, and $t \approx h$. With very thin pieces ($t \ll h$), the ratio of maximum frontal area to total area can be approximated as $A_{max}/S = 1/2$. For pieces of commensurate depth and height, the area ratio simplifies to

$$\frac{A_{max}}{S} = \frac{AR}{2 + 4AR} \tag{14}$$

which varies between 1/6 and 1/4 depending upon the shape. Thus, the upper bound of $A_{max}/S = 1/2$ is provided by thin pieces, while the lower bound of $A_{max}/S = 1/6$ is provided by a cube.

Combining the two geometric bounding analyses provides the desired bounds for the effective aerodynamic area of dynamic bluff bodies. The upper bound (largest drag) takes a value of $(A/S)_{ub} = 1/2$, and is characterized by thin, stable shapes. The lower bound (lowest drag) takes a value of $(A/S)_{lb} = 1/12$, and is characterized by rotating cubes. Note that these extremes refer to the drag *coefficient*, and are the result of both the dynamics and the accounting required to use total area as the reference area. A cube and an equivalent thin sheet will still produce the same drag *force* due to the larger total area for the cube. These extremes are examined in Fig. 6 using two of the shapes from the gallery in Fig. 1. Unconstrained 6-DOF trajectories were computed for SSLV tile gap filler, an extremely thin parallelepiped with aspect ratios between 3 and 6, and also for a cube shape. Both sets of trajectories were computed for release conditions of Mach 2.5. As expected, the cube shape shows a drag coefficient approaching the lower bound, and there is little variation. The thin gap filler results approach the upper bound for drag coefficient, and show a large variation as the debris rotates between bluff-body and edge-on orientations.

The results presented in Fig. 6 highlight that the upper bounding curve for drag coefficient can be conservative. Recall that the drag prediction itself is a conservative upper bound based on an infinite aspect ratio body. This, combined with the accounting of total area

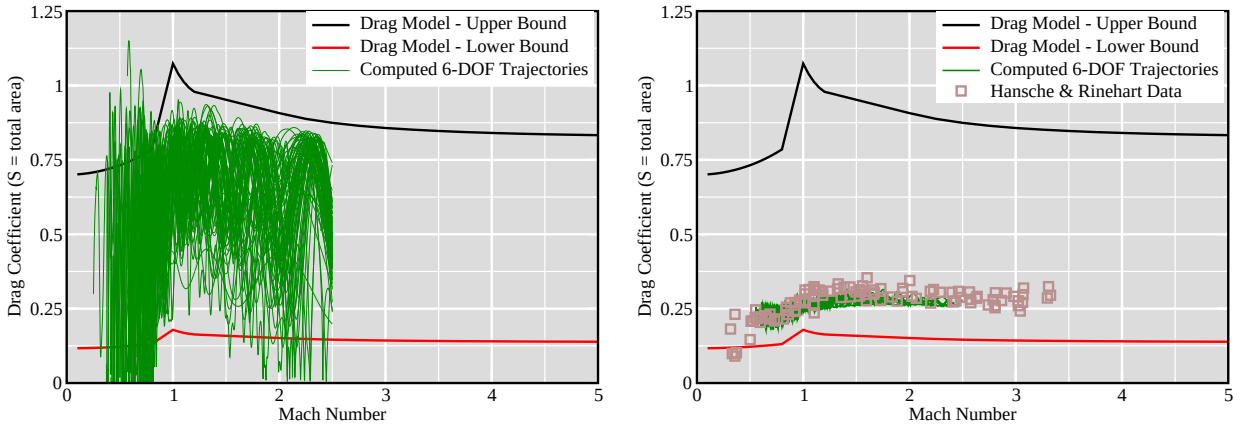

(a) Gap Filler (b) Cube

Figure 6: Drag model compared to computed 6-DOF trajectories for two geometric extremes. Release Mach number is 2.5. Range data for cubes from [3].

used in the drag coefficient leads to the conservative estimate. If there is a knowledge of the dimensions of the body, then an improved estimate can be constructed using the parameter $t/h \in [0, 1]$. The following variation for the upper bounding curve is proposed

$$\left(\frac{A}{S}\right)_{ub} = \frac{1}{4}\left[2 - \sqrt{\frac{t}{h}}\right] \tag{15}$$

This improvement is included in Fig. 7 for the cube shape ($t/h = 1$). Note that the intention is to provide an equal increment between the lower and upper boundaries and the nominal trajectory data, in order to facilitate the development of nominal and stochastic models.

The analysis presented above incorporates corrections based solely on the geometry of the shape. A general method of predicting the dynamics (tumbling, small oscillations, large oscillations, ...) under general flow conditions is not available, and as such a dynamic correction to the drag coefficient is not offered.

2.5 Examples

The following examples demonstrate the predictive capability of the drag coefficient modeling against several of the shapes from Fig. 1 under various ascent conditions. While examining the variation of drag coefficient with Mach number is useful, an additional metric is the prediction of velocity against distance during deceleration in a uniform flowfield. This integrated velocity accounts for the drop in dynamic pressure during an unconstrained trajectory for a debris piece. Figure 8 presents the drag coefficient and integrated velocity variation for an acreage foam divot ($t/h \equiv t/D = 0.25$) released at Mach 2.5. Computed trajectories are compared to the bounding model curves. A similar comparison for a Mach

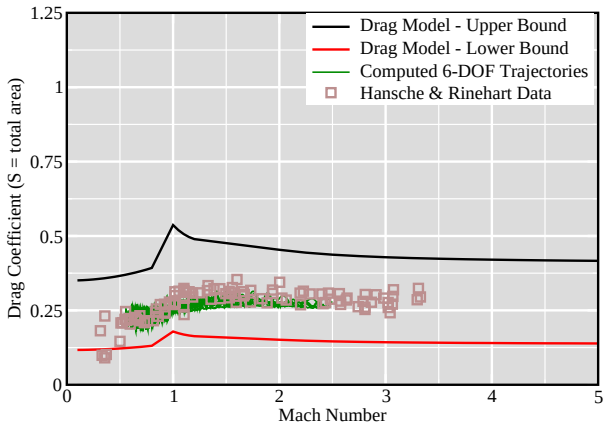

Figure 7: Corrrected drag model (Eqn. 15) compared to 6-DOF trajectories for a cube shape ($t/h = 1$). Release Mach number is 2.5. Range data for cubes from [3].

5.0 release is presented in Fig. 9, and for an idealized frustum shape released at Mach 2.5 in Fig. 10. An idealized foam frustum is known to be stable in a bluff-body orientation at Mach 2.5, and hence the integrated velocity for the computed 6-DOF trajectories lie towards the upper-boundary model results. This result provides a positive consistency check on the analysis.

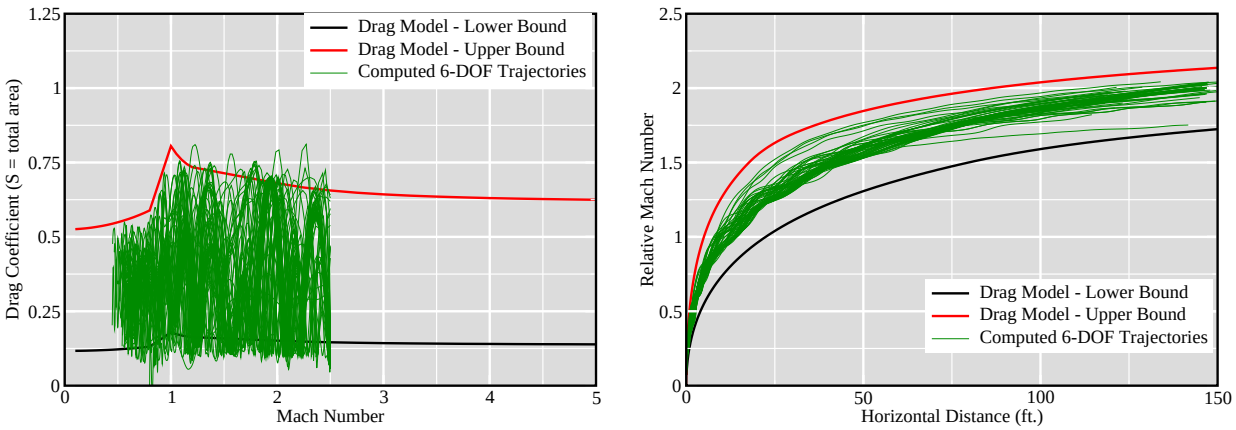

(a) Drag Coefficient (b) Relative Velocity

Figure 8: Drag model compared to computed 6-DOF trajectories for an acreage divot ($t/h \equiv t/D = 0.25$). Release Mach number is 2.5.

Similar comparisons for various ice debris shapes (hemisphere, feedline bellows, quarter-sphere) are presented in Figs. 11-13 for subsonic and supersonic release conditions.

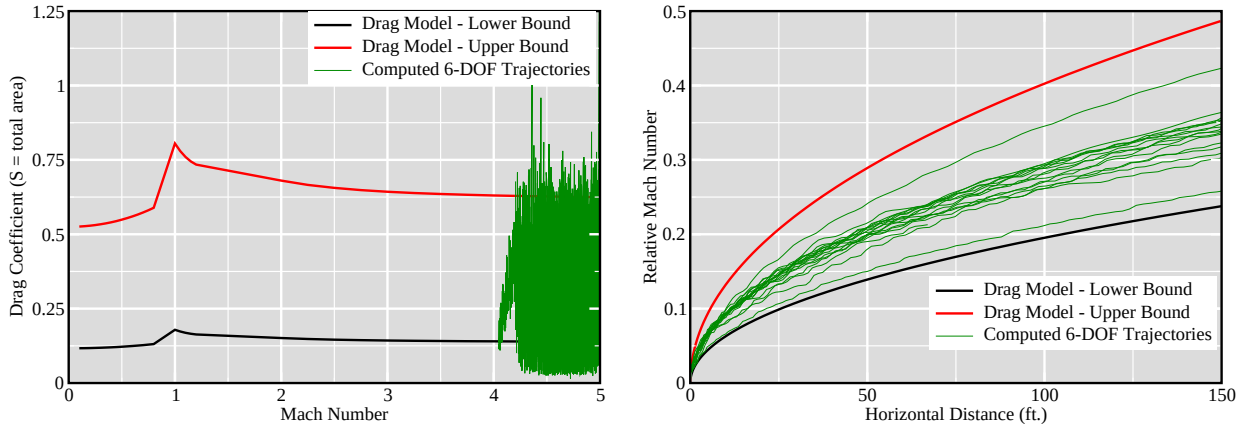

(a) Drag Coefficient (b) Relative Velocity

Figure 9: Drag model compared to computed 6-DOF trajectories for an acreage divot ($t/h \equiv t/D = 0.25$). Release Mach number is 5.0.

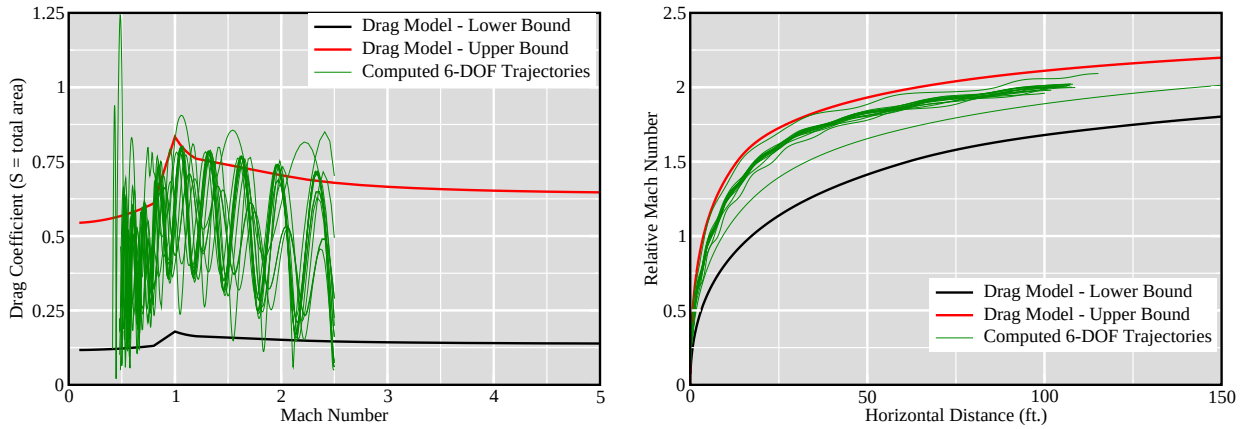

(a) Drag Coefficient (b) Relative Velocity

Figure 10: Drag model compared to computed 6-DOF trajectories for an idealized frustum divot ($t/h \equiv t/D = 0.2$). Release Mach number is 2.5.

2.6 Comparison with Frustum Drag Model

In [1] a drag model tailored to the dynamic behavior of ET acreage foam divots is described. This drag model is based on the aerodynamics of idealized frustum shapes with a bevel angle of 45°. The conversion of the geometric properties for a general acreage foam divot to an area scaling which can be used with the frustum drag model is complicated, however, this procedure can provide a more refined estimate of the drag behavior than the generic bluff-body analysis described herein. Figure 14 presents a comparison of the integrated velocity prediction for the generic model and the refined frustum model for the flange

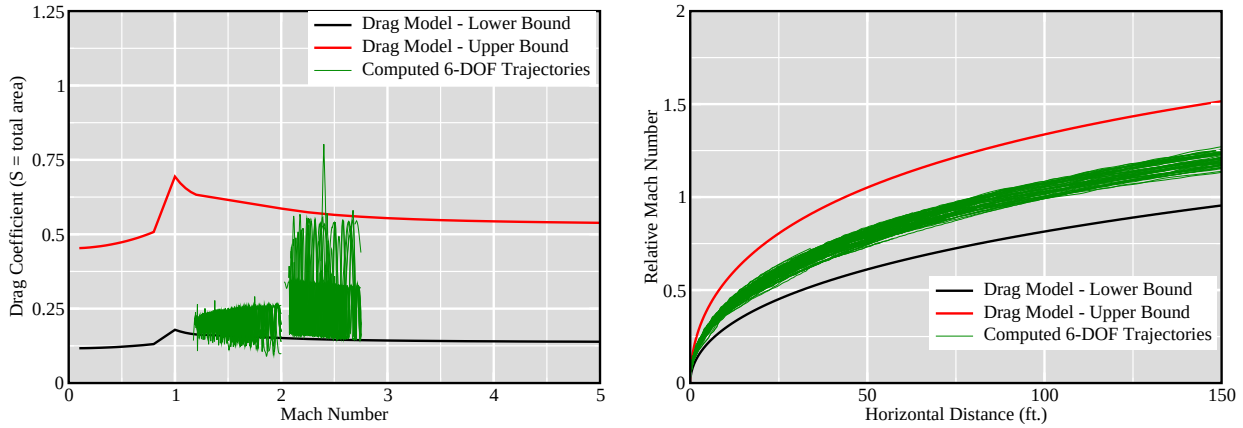

(a) Drag Coefficient (b) Relative Velocity

Figure 11: Drag model compared to computed 6-DOF trajectories for an ice hemisphere ($t/h \equiv t/D = 0.5$). Release Mach number is 2.75.

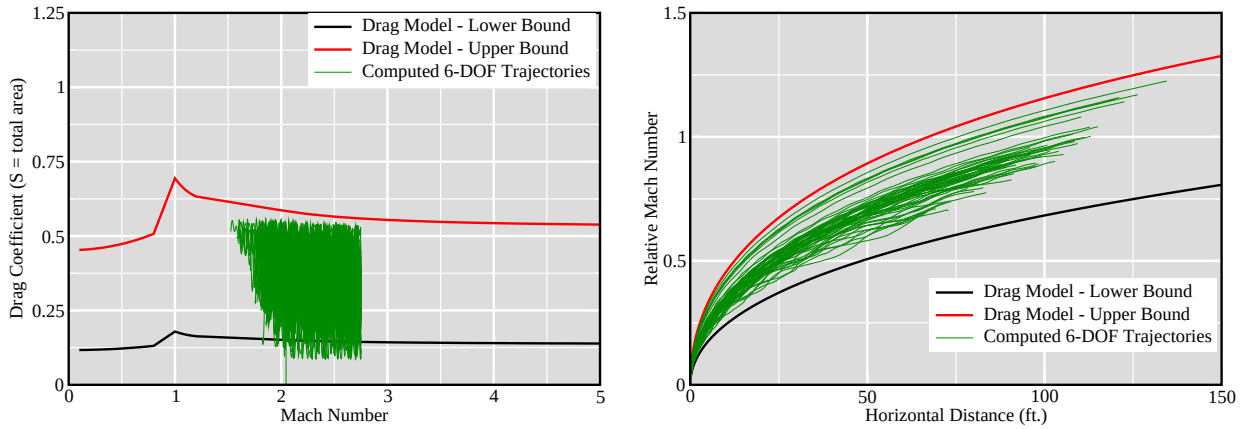

(a) Drag Coefficient (b) Relative Velocity

Figure 12: Drag model compared to computed 6-DOF trajectories for a 2 inch long feedline bellows ice shape ($t/h \approx 0.5$). Release Mach number is 2.75.

and idealized frustum foam divots. The uncertainty in the predictions using the frustum drag model are lower in both cases.

2.7 Summary

The upper and lower bounding curves for the approximate drag model show a very good predictive capability for a variety of shapes and dynamic trajectories. The nominal behavior of the computed 6-DOF trajectories is well represented by the average of the upper and

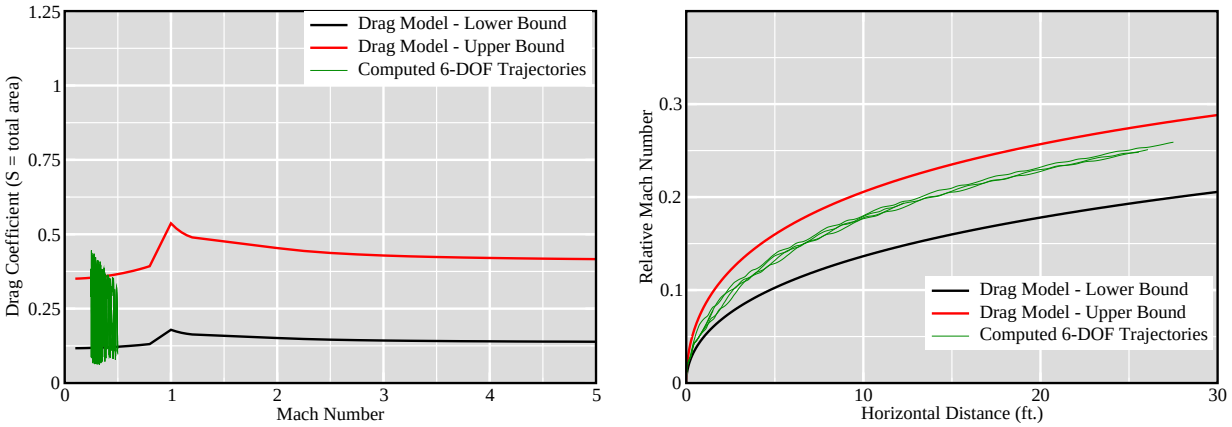

(a) Drag Coefficient (b) Relative Velocity

Figure 13: Drag model compared to computed 6-DOF trajectories for an ice quarter-sphere ($t/h = 1.0$). Release Mach number is 0.5.

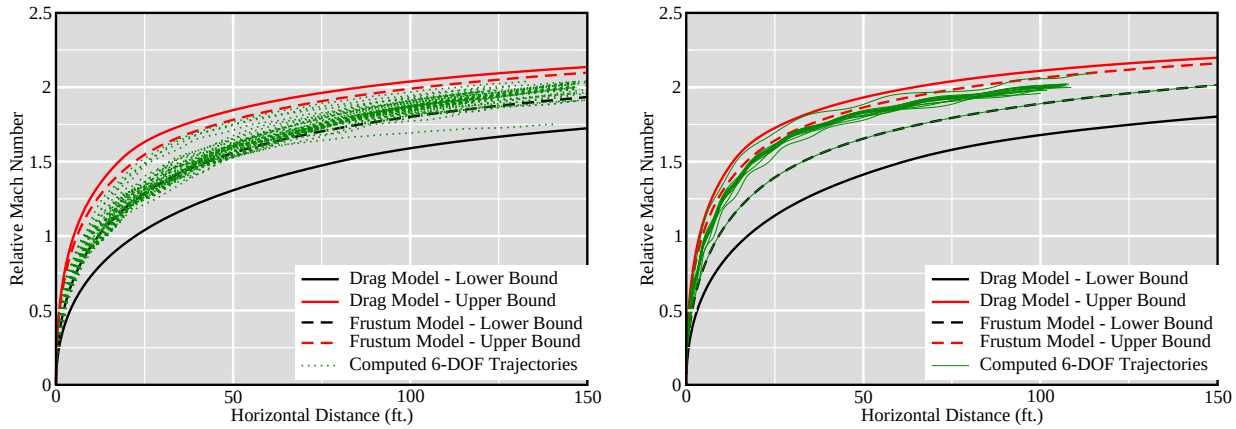

(a) Flange (b) Ideal Frustum

Figure 14: Drag model compared to computed 6-DOF trajectories and frustum drag model for foam acreage divots. Release Mach number is 2.5.

lower bounds. A stochastic analysis can easily be supported by assuming an appropriate probability density function between the bounding curves.

References

[1] Murman, S.M., Aftosmis, M.J., and Rogers, S.E., "Characterization of Space Shuttle Ascent Debris Aerodynamics Using CFD Methods," AIAA Paper 2005-1223, January 2005.

[2] Ames Research Staff, "Equations, Tables, and Charts for Compressible Flow," NACA Report 1135, 1953.

[3] Hansche, G.E. and Rinehart, J.S., "Air Drag on Cubes at Mach Numbers 0.5 to 3.5," *Journal of the Aeronautical Sciences*, 19:83–84, 1952. Also *Fluid-Dynamic Drag*, Hoerner, S.F., 1965. pg. 16–14.